Variations of strain-drops of aftershocks of the 1999 İzmit and Düzce earthquakes around the Karadere-Düzce branch of the North Anatolian Fault

Wenzheng Yang,[1] Zhigang Peng[2] and Yehuda Ben-Zion[1]

[1]*Department of Earth Sciences, University of Southern California, Los Angeles,* CA 90089-0740, *USA. E-mail: wenzheny@usc.edu*
[2]*School of Earth and Atmospheric Sciences, Georgia Institute of Technology, Atlanta,* GA 30332-0340, *USA*

SUMMARY
We estimate the strain-drops of 7498 aftershocks of the 1999 İzmit and Düzce earthquakes using *P* waveforms recorded by a local seismic network along the Karadere-Düzce branch of the North Anatolian fault in the 6 months following the İzmit main shock and evaluate the site effects of the various recording stations. The method is associated with separation of source, traveltime and station spectral terms and stacking results at several stages to enhance the signal-to-noise ratio. The strain-drops are obtained by fitting iteratively the separated source spectra of 201 nearest neighbouring events in different amplitude bins to the ω^{-2} source spectral model. The obtained strain-drops generally increase with depth between 3 and 10 km and remain approximately constant for the deeper section. A local shallow patch of seismicity north of the Karadere segment has relatively low strain-drop values. Along the relatively straight Karadere segment, the strain-drops are lower than along the geometrically complex bounding regions. In some sections, the range of strain-drop values decay with time from the İzmit and Düzce main shocks, whereas in others the values fluctuate within about constant ranges. The observed spatial variations of strain-drops can be explained by increasing normal stress with depth, along with the degree of geometrical complexity of different fault sections and the expected slip deficit at different depth sections. The seismic energy in the separated station spectra decreases overall with distance from the rupture zone and the spectra of various stations have three peaks at 6, 14 and 25 Hz. The spectral peak at 6 Hz is also observed in trapped waves studies and may be related to the damaged fault zone layer.

Key words: Earthquake dynamics; Earthquake source observations; Site effects; Seismicity and tectonics; Continental tectonics: strike-slip and transform.

1 INTRODUCTION

Observed seismograms result from a convolution of source, propagation path and site-instrument effects. Many useful source, path and site parameters can be obtained from recorded seismic waveforms after properly separating the various effects. One of the most important source parameters that can be computed through seismological methods is the reduction of the average elastic strain (ε) or stress (σ) over the earthquake rupture area. The strain- or stress-drops can be estimated from the shape of the earthquake source spectrum (i.e. corner frequency f_c) by assuming various source models (e.g. Brune 1970; Madariaga 1976; Aki & Richards 2002; Ben-Zion 2003). These parameters provide fundamental information on the physics of earthquake rupture and spatio-temporal evolutions of stress-strain conditions around earthquake faults.

Many methods have been developed in the past to isolate source signals from the observed seismograms. The most commonly used

one is referred to as the empirical Green function (EGF) method (e.g. Berckhemer 1962; Mueller 1985; Hough 1997). If waveforms of two neighbouring events with large magnitude difference are recorded by a common station, the source signal of the smaller event could be approximately treated as a delta function. Since the radiations from both events share very similar path and site responses, the relative source function of the larger event can be obtained by deconvolving its seismic record with that of the smaller event. However, the application of the EGF method is somewhat limited because it requires two events with close locations and with large size difference. In addition, the deconvolution operator may introduce some artificial signals if the noise level of the smaller event is high. Another group of methods take advantage of the fact that multiple events are recorded by multiple stations and separate the relative source, path and station terms by solving a series of linear equations (e.g. Andrews 1986; Boatwright *et al.* 1991). However, the obtained results may not be stable due to the existence of random
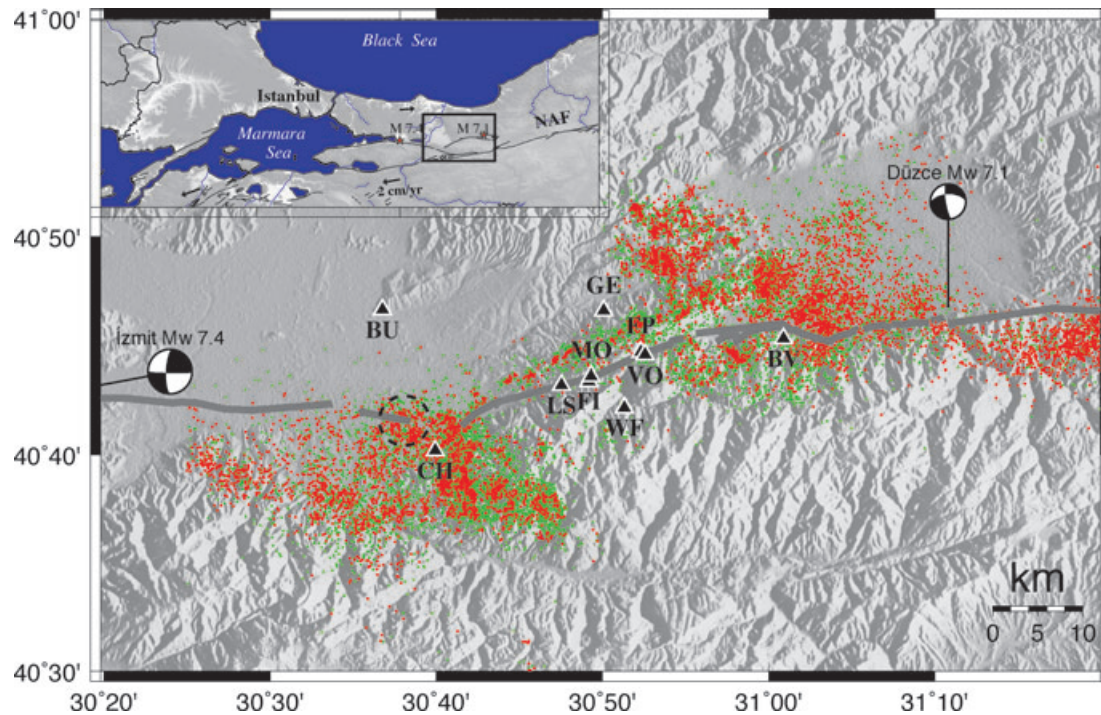
Figure 1. Epicentral distribution of 18 556 earthquakes (green and red dots) along the Karadere-Düzce branch of the North Anatolian Fault. The strain-drops of 7498 events (red points) are estimated in this study. The grey lines denote observed rupture traces of the İzmit and Düzce main shocks and the black triangles are the 10 seismic stations. Focal mechanisms of both the İzmit and Düzce main shocks point to their epicentres. The events inside the black circle are used with 201 nearest-neighbours to illustrate the separation of the source, station and traveltime terms (Fig. 3a), to stack the separated source terms (Fig. 3b) and to obtain the best fitting strain-drop (Fig. 4). The inset map shows the location of the study area (black rectangle) in a large-scale regional map.

noise. Warren & Shearer (2002) introduced a stacking technique to enhance the common features of signals and decrease the effect of random noise. Such method has been applied to obtain reliable source properties of small earthquakes at many regions (Prieto *et al.* 2004; Shearer *et al.* 2006; Allmann & Shearer 2007).

The above developments notwithstanding, basic aspects of source and sites effects remain unclear, primarily because of the limited direct information and considerable uncertainties at both ends of the source-observation system. Several sources of uncertainties contribute to the large scatter and discrepancies of the available results. First, estimations of the corner frequency, stress/strain-drop, rupture velocity and seismic energy depend on the high-frequency part of the seismic spectra, where correcting for attenuation and other path effects may be difficult. Second, previous studies have been done either in one location with a single or a few stations (e.g. Abercrombie 1995), at a large region with a mixture of tectonic environments (e.g. Shearer *et al.* 2006) or using combinations of data associated with different studies (e.g. Ide & Beroza 2001). Systematic analysis of large seismic waveform data recorded by multiple stations in nearby regions can provide better constraints on earthquake source properties and site effects.

In this study, we apply an iterative stacking technique to separate source, propagation and site effects in a large seismic data set recorded along and around the Karadere-Düzce branch of the North Anatolian Fault (NAF) during the 1999 İzmit and Düzce earthquake sequences in Turkey. The earthquakes (Fig. 1) are highly concentrated in space (within ∼10-km-wide 100-km-long region around the Karadere-Düzce branch of the NAF) and time (within ∼6 months). Moreover, the data were recorded over a period that includes both the early post-main shock and final pre-main shock stages of large earthquake cycles (in relation to the İzmit and Düzce

events, respectively). We focus on analysis of *P* waveforms and estimate strain-drops of about 7500 earthquakes and site effects of stations with various distances from the rupture zones of the İzmit and Düzce main shocks. The derived strain-drops are generally higher along fault sections with larger geometrical complexity, and they increase with depth. The seismic energy associated with site effects includes spectral peaks around 6, 14 and 25 Hz and is largest at a station that was installed within the rupture zone of the İzmit earthquake.

2 DATA AND PREPROCESSING

2.1 Data

A temporary PASSCAL network of 10 short-period seismic stations was deployed along and around the Karadere-Düzce branch of NAF a week after the 1999 August 17 M_W7.4, İzmit, Turkey, earthquake (Fig. 1). All stations had REFTEK recorders and three-component L22 velocity sensors with a sampling frequency of 100 Hz (Seeber *et al.* 2000; Ben-Zion *et al.* 2003). This network operated for 6 months and recorded approximately 26 000 events, including the 1999 November 12 M_W7.1, Düzce earthquake. In this study, we use a subset of 18 556 events that are within 30 km of the network (Peng & Ben-Zion 2004). The employed events have magnitudes in the range between −0.1 and 3.9. The horizontal location errors are generally less than 1 km around the centre of the network and 1–2 km near the margins. The vertical location errors are somewhat larger. Additional details on the seismic experiment and data set are given by Seeber *et al.* (2000) and Ben-Zion *et al.* (2003).
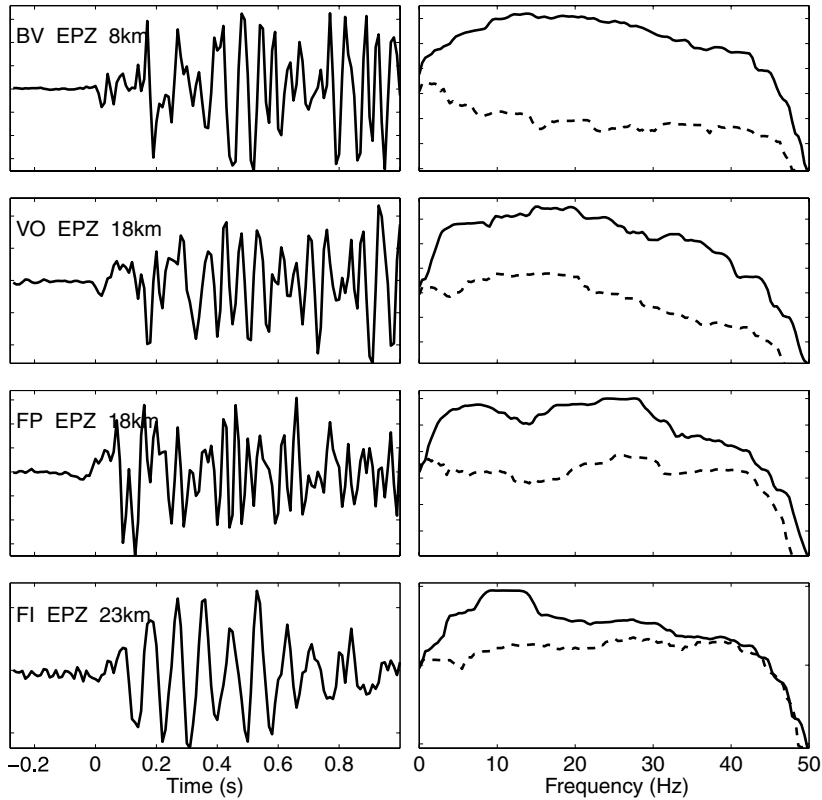
Figure 2. Example results based on a 2000 Jan 20 M_L 2.0 earthquake recorded by four stations (BV, VO, FP and FI). The left-hand panels show the velocity waveforms around the *P*-wave window. The station name, component and epicentral distance are marked on the left-hand side. The right-hand panels show the $\log_{10}$ displacement spectra for both signal (solid line) and noise (dashed line).

2.2 Pre-processing

We analyse the *P* waves recorded on the vertical component of the short-period instruments. The preprocessing steps are as follows. We remove the mean and trend from each seismogram, correct the instrumental response and convert the waveforms from velocity to displacement records. We also remove traces that are clearly clipped. These analysis steps are done using Matlab functions in the CORAL package for seismic waveform analysis (Creager 1997). We take the signal window to be 0.28 s before and 1.0 s after the picked *P* arrival and take a background noise window to be with the same length before the picked *P* arrival. The displacement spectra for the noise and signal windows are computed using a multitaper algorithm (Thomson 1982; Park *et al.* 1987). We require the signal-to-noise ratio (SNR) of the obtained spectra in the frequency band 2.35–20 Hz to be larger than 3.0. We also require, for further analysis, the minimum number of qualified observed waveforms for an event to be larger than 3. After the data preprocessing, we have 48 580 *P*-wave spectra from 7498 events. Examples of waveforms and corresponding signal and noise spectra for one event at several stations are shown in Fig. 2.

3 METHOD

We use a method that generally follows the procedure of Shearer *et al.* (2006) to estimate potency values and strain-drops of earthquakes in a large regional data set. The method involves spectral stacking at several steps to increase the stability of the results and is associated with three major analysis stages. In the first stage, we separate iteratively the source, traveltime and station spectra, using for each earthquake the observed data of its N nearest neighbour events (here $N = 200$). In the second stage, we bin the separated source terms in different amplitude ranges and stack the source spectra in each bin. In the third stage, we fit the stacked source spectra of each bin with a theoretical source model (we assume ω^{-2} spectral decay) and obtain best-fitting earthquake strain-drops.

Our method differs from the studies of Shearer *et al.* (2006) and related works (e.g. Prieto *et al.* 2004; Allmann & Shearer 2007) primarily by using in the analysis strain-based quantities (potency and strain-drops) rather than the more traditional stress-based quantities (moments and stress drops). This makes the results independent of assumed rigidity values in the source regions. As discussed by Ben-Zion (2003, 2008), the rigidity values vary rapidly and are hence poorly defined in the space-time windows associated with earthquakes. Moreover, the rigidity values in the source volumes do not affect the seismic radiation in the surrounding elastic solid and can thus be assigned arbitrarily. For these reasons, we prefer to use parameters associated with strain-based quantities. Additional details on the various analysis procedures are given below.

3.1 Iterative separation of source, station and traveltime spectra

In the log-frequency domain, the observed displacement spectra can be expressed as

$$d_{ij} = e_i + t_{ij} + s_j + r_{ij}, \tag{1}$$

where d_{ij} is the observed displacement spectrum of the *i*th event recorded by the *j*th station, e_i is the source term of the *i*th event, s_j is the station term of the *j*th station, t_{ij} is the traveltime term for the event-station pair and r_{ij} is a residual term. Assuming that the

attenuation is associated with a constant value, t_{ij} can be discretized into a sequence of k intervals that cover the range of all possible traveltime terms (Shearer *et al.* 2006).

In this procedure, we consider spectral data in a frequency range between 2.35 and 45 Hz, which is wider than the range used in the subsequent analysis steps. We discretize the traveltime term t_{ij} at 1.0 s increments and set the range of acceptable residuals r_{ij} to be within $[-1.0 \ -1.0]$ nm Hz^{-1}. Each event is analysed jointly with its nearest $N = 200$ events. The iterative separation of the different terms of Eq. 1 for each group of $N + 1$ events is done as follows:

(1) We set the initial source, traveltime and residual terms at the first iteration to be zero. We solve for the initial station term as the stacked value of the observed displacement spectra,

$$s_j^1 = \frac{1}{m} \sum_{i=1}^{m} d_{ij}, \tag{2}$$

where $m \leq N$ is the total number of events recorded by the *j*-th station.

(2) We solve for the source term at the *p*-th iteration ($p = 2,3,\ldots$) using

$$e_i^{(p)} = \frac{1}{n} \sum_{j=1}^{n} \left[d_{ij} - s_j^{(p-1)} - t_{(k)ij}^{(p-1)} - r_{ij}^{(p-1)} \right], \tag{3}$$

where n is the total number of stations which recorded the *i*-th event and the subscript k denotes the appropriate discrete traveltime for various source–station pairs ij.

(3) We solve for the traveltime term at the *p*-th iteration ($p = 2,3,\ldots$) using

$$t_k^{(p)} = \frac{1}{N_k} \sum \left[d_{ij} - e_i^{(p)} - s_j^{(p-1)} - r_{ij}^{(p-1)} \right], \tag{4}$$

where N_k is the total number of event–station pairs within the *k*-th traveltime interval ($k = 1,2,\ldots$).

(4) We solve for the station term at the *p*-th iteration ($p = 2,3,\ldots$) as

$$s_j^{(p)} = \frac{1}{m} \sum_{i=1}^{m} \left[d_{ij} - e_i^{(p)} - t_{(k)ij}^{(p)} - r_{ij}^{(p-1)} \right]. \tag{5}$$

(5) We solve for the residual term at the *p*-th iteration ($p = 2,3,\ldots$) as

$$r_{ij}^{(p)} = d_{ij} - e_i^{(p)} - s_j^{(p)} - t_{(k)ij}^{(p)}. \tag{6}$$

If the mean value of r_{ij} is outside the acceptable residual boundaries, the corresponding waveform will be dropped from subsequent iterations. If the corresponding event has less than three waveforms, it will be dropped from further analysis.

(6) We calculate the following sums of the absolute difference values: $\sum_i |e_i^{(p)} - e_i^{(p-1)}|$, $\sum_j |s_j^{(p)} - s_j^{(p-1)}|$, $\sum_i |t_{(k)ij}^{(p)} - t_{(k)ij}^{(p-1)}|$. The iteration stops when each sum value is less than a very small number (e.g. 1×10^{-4}), and otherwise it returns to step 2.

As in the study of Shearer *et al.* (2006), the analysis steps discussed above usually converge and terminate in 2–3 iterations. An illustration of the separated source, station, traveltime and residual terms of 201 nearest neighbouring events, with locations inside the black circle of Fig. 1, are shown in Fig. 3(a).

3.2 Stacking of source terms with similar amplitudes

The separated 201 source spectra obtained by the procedure of Section 3.1 can have large fluctuations (left-hand panel in Fig. 3b),

which are at least partially due to errors from random noise. To capture the common features of the neighbourhoods of earthquake sources that are analysed jointly, we follow Shearer *et al.* (2006) and stack the source spectra over 0.2 logarithmic amplitude bins. The shapes of the obtained stacked source spectra at the different amplitude bins are relatively smooth (right-hand panel in Fig. 3b). As expected from the Gutenberg–Richter frequency-size statistics of earthquakes, the spectral shapes for bins at lower amplitudes are stacked from a larger number of individual spectra than those at higher amplitude bins. This explains why the stacked source spectra for the larger events still have some shape irregularities at high frequency. However, larger events generally have higher SNR, and their corner frequencies are better contained within the frequency range (2.35–20 Hz) analysed in our study.

3.3 Fitting source spectra with theoretical model

In this analysis stage, the binned source spectra are fitted with a theoretical source model, and a near-source common EGF is simultaneously removed from the results. We use the theoretical source model of Brune (1970)

$$u(f) = \frac{\Omega_0}{1 + (f/f_c)^n}, \tag{7}$$

where $u(f)$ is the displacement spectra, f_c is the corner frequency and Ω_0 is the zero frequency asymptote (proportional to the scalar seismic potency P_0 and scalar seismic moment $M_0 = \mu P_0$ with μ being a nominal rigidity at the source). Since the binned source spectra are relatively flat at the low frequency range (Fig. 3b), we use the mean amplitude of the first four points (2.35–3.53 Hz) of the source displacement spectra to estimate Ω_0.

The corner frequency f_c can be related to the scalar seismic moment M_0 and seismic potency P_0 by assuming a circular rupture model (Madariaga 1976; Abercrombie 1995; Prieto *et al.* 2004; Shearer *et al.* 2006; Allmann & Shearer 2007) with a constant rupture velocity of 0.9 times the shear wave velocity β,

$$f_c = \frac{0.42\beta}{(M_0/\Delta\sigma)^{1/3}} = \frac{0.42\beta}{(P_0/\Delta\varepsilon)^{1/3}}, \tag{8}$$

where $\Delta\sigma$ and $\Delta\varepsilon$ are the stress- and strain-drops of the earthquake, respectively.

Since the zero frequency asymptote Ω_0 obtained from the separated source spectrum is a relative value, it does not provide information on the corresponding absolute seismic potency. To calibrate the average potency in each amplitude bin with the corresponding average local magnitude, we use the empirical potency–magnitude equation of Ben-Zion & Zhu (2002):

$$P_0 = 10^{0.0612M_L^2 + 0.988M_L - 4.87}. \tag{9}$$

Using eqs (7)–(9), we fit the source spectra with a procedure involving only variations of the assumed strain-drops for the groups of analysed events (Fig. 4). This is done as follows:

(1) We set a range of possible values of strain-drops $3 \times 10^{-6} \leq \Delta\varepsilon \leq 1 \times 10^{-2}$ (Fig. 4a). Assuming a nominal rigidity of 30 GPa, this corresponds to stress drops in the range 0.09–300 MPa. The range of allowed $\log_{10}$ strain-drops is divided to intervals of 0.0035, giving a total number of 1000 strain-drops values. For each possible strain-drop value, we compute the theoretical source spectra for each bin using the ω^{-2} model ($n = 2$ in eq. 7).

(2) We calculate the difference between the theoretical source spectrum for a given strain-drop value and stacked source spectra
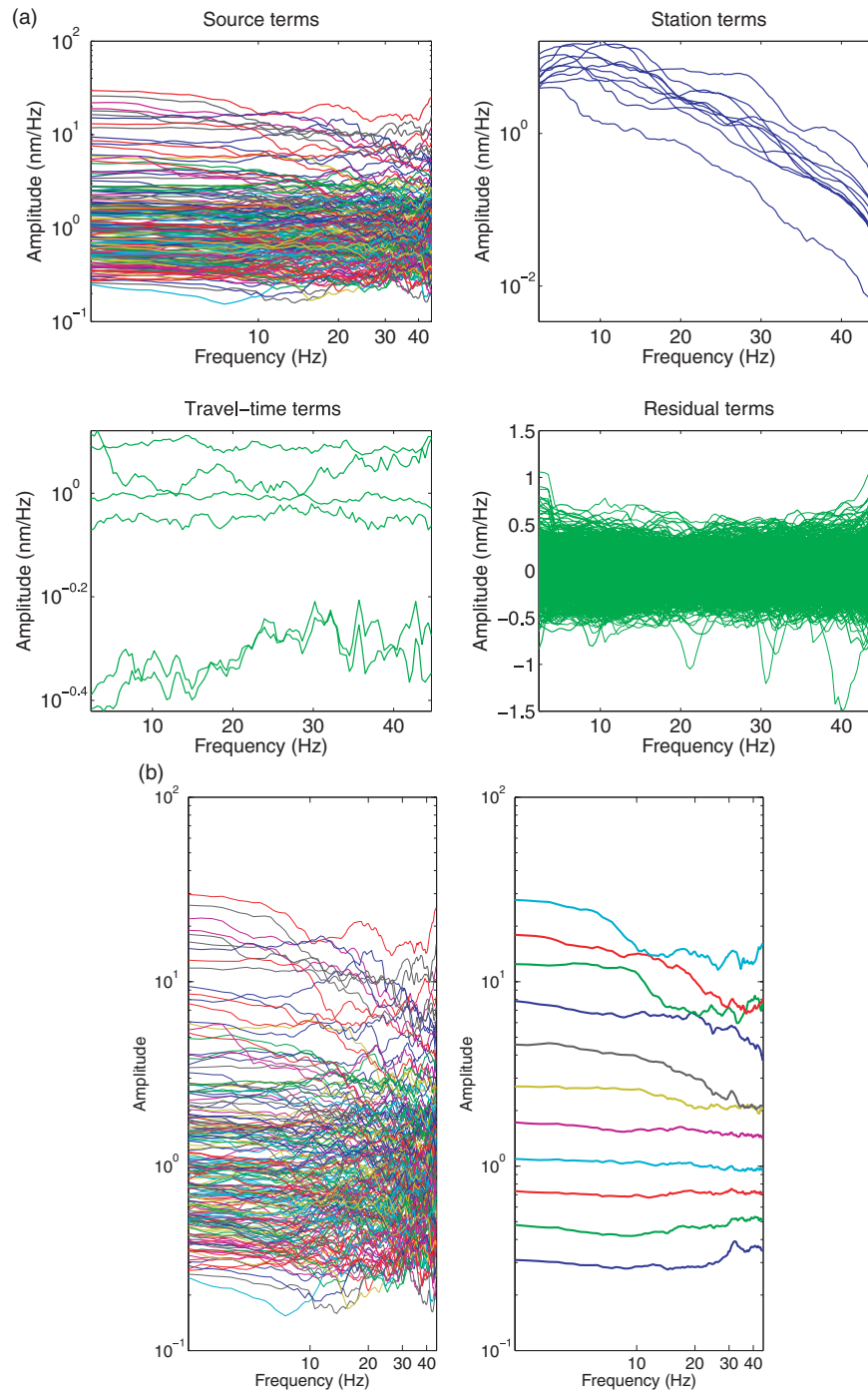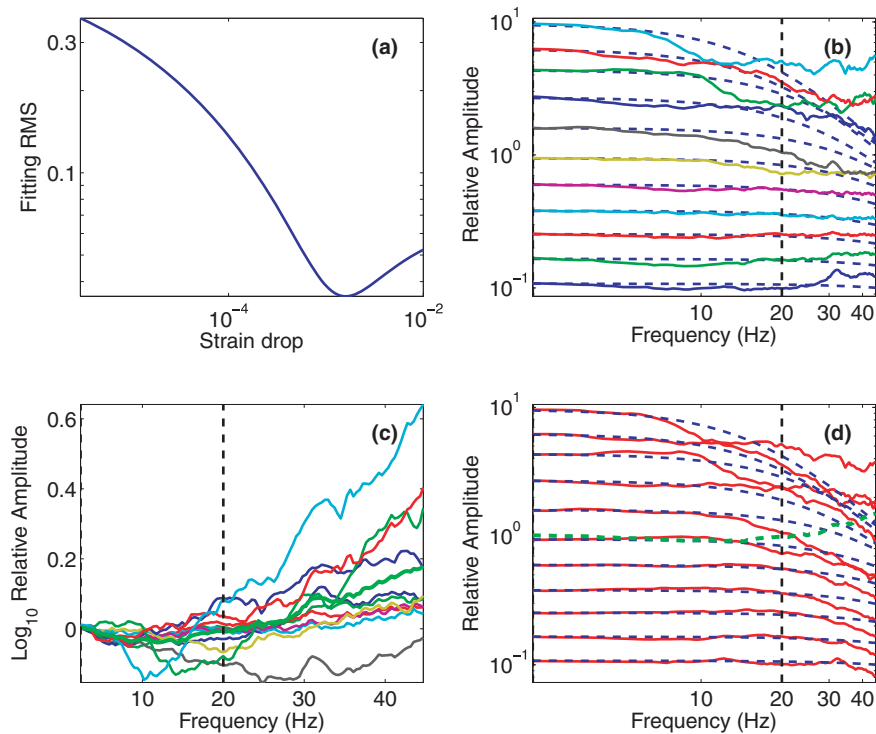
Figure 3. (a) Illustration of the source, station and traveltime terms separation for 201 nearest neighbouring events. (b) Illustration of separated source spectra and the corresponding stacking. The left-hand panel shows the separated source spectra for 201 nearest neighbouring events. The right-hand panel shows the stacked source spectra with 0.2 logarithmic amplitude increments.

at each amplitude bin (Fig. 4b). We then stack the differences of all amplitude bins to obtain a single common EGF (Fig. 4c).

(3) We compute the root mean square (rms) misfit, which is the sum of differences between the theoretical source spectra and the EGF-corrected source spectra for all amplitude bins over the employed frequency band (2.35–20 Hz). The value of $\Delta\varepsilon$ that provides the minimum RMS misfit (Figs 4a and d) is selected as a best-fitting strain-drop for the group of events.

4 RESULTS

For each of the 7498 events that satisfy the discussed quality criteria (Section 2.2), we use the above procedure to derive potency and strain-drop values with both constant and depth-variable velocity models. About 95 per cent of the derived $\log_{10}$ strain-drops are in the range from -4.3 to -2.6 (corresponding to 1.5–75 MPa stress-drops assuming a nominal rigidity of 30 GPa), with a mean

Figure 4. Illustration of the strain-drop fitting for an event and its 200 nearest-neighbours. (a) The fitting rms curve vs $\log_{10}$ strain-drop over the range between −5.0 and −2.0. (b) The separated source spectra are binned with 0.2 increments in magnitude (solid colour lines). The theoretical source spectra with the strain-drop as unknown parameter are shown in blue dashed lines. The vertical dashed line marks the upper limit of the fitting frequency. (c) The difference between the theoretical and separated source spectra in each bin (colour curves) and the stacked difference (bold green curve) giving the common EGF. (d) The EGF-corrected source spectra (red curves) and the theoretical source spectra (blue dashed curves). The best-fitting strain-drop corresponds to the minimum fitting rms value in (a).

$\log_{10}$ value of −3.5 (9.5 MPa). Details of the obtained results are presented below.

4.1 Spatial variations of strain-drops

Fig. 5a shows the best-fitting strain-drops for the analysed 7498 events (red dots in Fig. 1). The results are derived by assuming a constant shear wave velocity $\beta = 3.5$ km s^{-1} (i.e. a constant P-wave velocity $\alpha = 6$ km s^{-1}, and $\alpha/\beta = \sqrt{3}$). Fig. 5b illustrates the goodness of obtained source spectra and strain-drop fitting using 10 $M_L \approx 2.1$ events at different locations inside the study region (marked as cyan circles in Fig. 5a). For each event, we plot the EGF-corrected stacked source spectra of earthquakes with different spectral amplitude bins belonging to the $N = 201$ neighbourhood of the selected events (panels in Fig. 5b), along with the theoretical source spectra of the best-fitting strain-drop (dashed blue lines) and the common EGF (dashed green line). As in Fig. 4(b), the stacked source spectra are relatively smooth and generally match well the theoretical curves associated with the best-fitting strain-drops. As shown in Fig. 5(a), the strain-drops vary smoothly for nearby events, as expected from the smearing effects of the 201 nearest neighbouring approach. However, there are clear variations of strain-drops along the different fault traces in the study area. Based on the overall observed patterns of the strain-drops and aftershock locations, we divide the examined region into four sections and discuss the patterns in each section separately.

Section I is between longitudes 30°20′ and 30°40′, where the strike of the surface trace of the NAF is along the E–W direction. Most aftershocks in this section were generated by the İzmit main

shock, and they are associated generally with depth larger than 5 km (Fig. 6). The strain-drops in this section are relatively high. Section II is between longitudes 30°40′ and 31°, where the fault strike of the Karadere segment is N71°E. Most aftershocks were generated by the İzmit main shock, and they form a linear band (line AB), which is parallel to the surface trace of the Karadere segment with a 2–3 km offset to the northwest as the Karadere segment steeply dips to the NW. Additional aftershocks occurred on the SE side of station CH and NE side of station GE, which are far from the surface ruptures of the İzmit main shock. Numerous aftershocks in this section occurred in the top few km of the crust (Fig. 6), and both the strain-drops and magnitude of the events are relatively low. Two small areas in this section (IIA and IIB in Fig. 5a) have clusters of events off the main fault with depths between 5 and 12 km and relatively high strain-drops (IIA and IIB in Fig. 6). Section III is defined as the region between longitudes 31° and 31°12′, and is associated with an overlap between the eastern end of the İzmit aftershock zone and the western part of the Düzce aftershock zone. The events in this section are generally deeper than 5 km (Fig. 6), and they are associated with relatively high strain-drops. Section IV is between longitudes 31°12′ and 31°20′, where the seismicity was primarily triggered by the Düzce main shock (Fig. 7). This section has the highest average strain-drops among all sections. Table 1 summarizes statistical features of the strain-drops in the different sections.

To illustrate further the spatial variations of earthquake strain-drops along the Karadere-Düzce branch of the NAF, we project the events onto a vertical plane intersecting the surface at line AB of Fig. 5a, which is parallel to the strike of the fault trace in the central
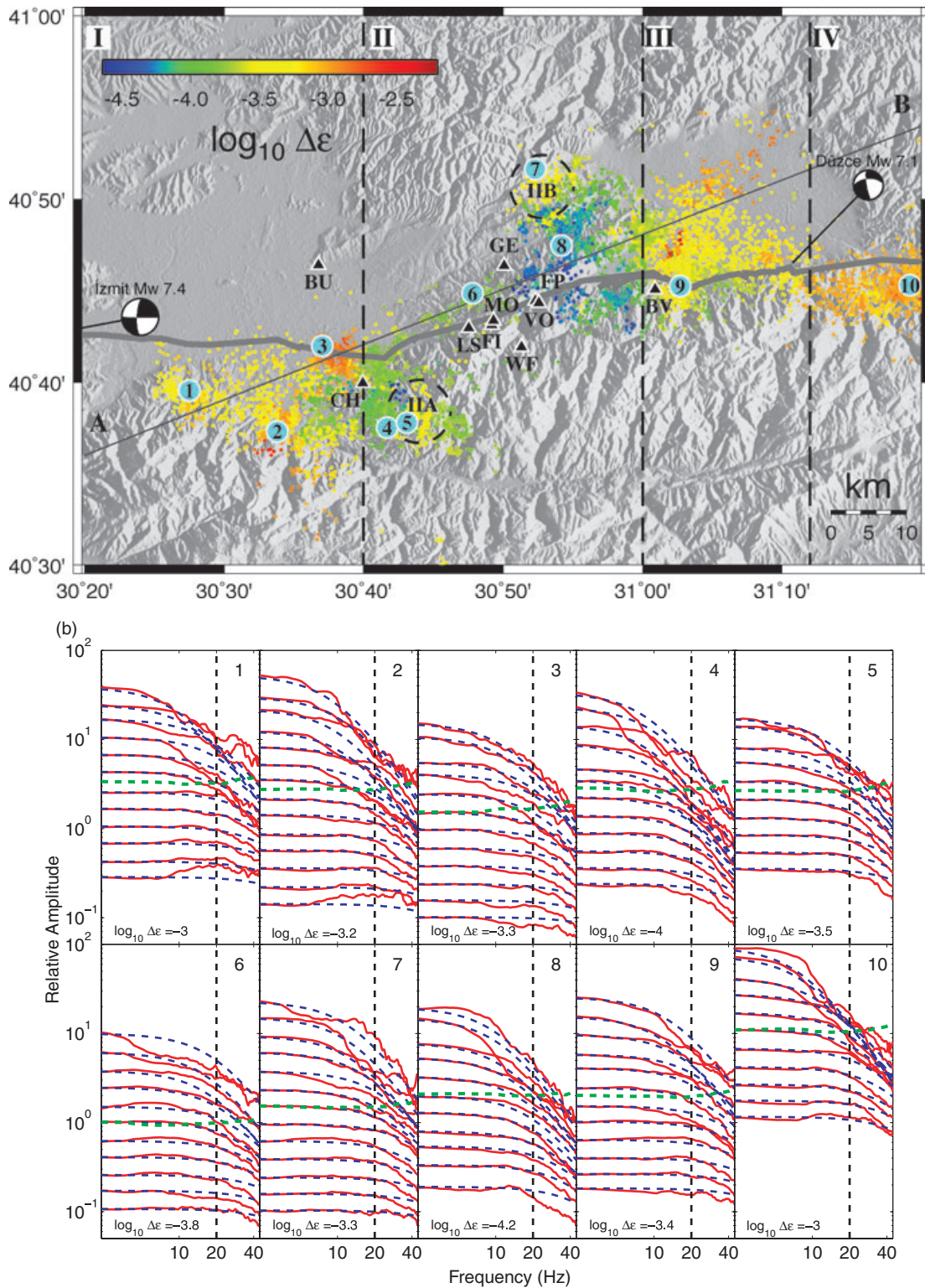
Figure 5. (a) A map of the best-fitting $\log_{10}$ strain-drops for 7498 aftershocks of the 1999 İzmit and Düzce earthquakes along the Karadere-Düzce branch of the North Anatolian Fault. The results are coloured in equal increments of $\log_{10} \Delta\varepsilon$ with colour bar at the upper-left-hand corner. Four subregions are separated by dashed lines with labels I, II, III and IV at the up-left-hand corners. Two subregions in section II with higher strain-drops are marked with circles and labelled as IIA and IIB. The black triangles represent the 10 stations. The seismicity projected along line AB of N71°E (parallel to the fault strike of the Karadere segment) is shown in Figs 6 and 7. (b) The EGF-corrected stacked source spectra (red curves) for each of the 10 $M_L \approx 2.1$ events marked in panel (a) with its 200 nearest-neighbours and the theoretical source spectra (blue dash curves) associated with the best-fitting strain-drop. In each panel, the number at the top-right-hand corner corresponds to the appropriate number within the cyan circle in panel (a), and the best-fitting $\log_{10}$ strain-drop is marked at the bottom-left-hand corner. For a better comparison of the spectral curves, the various spectral amplitudes are shifted according to the median event magnitude in each panel. Other symbols and notations are the same as in Fig. 4.
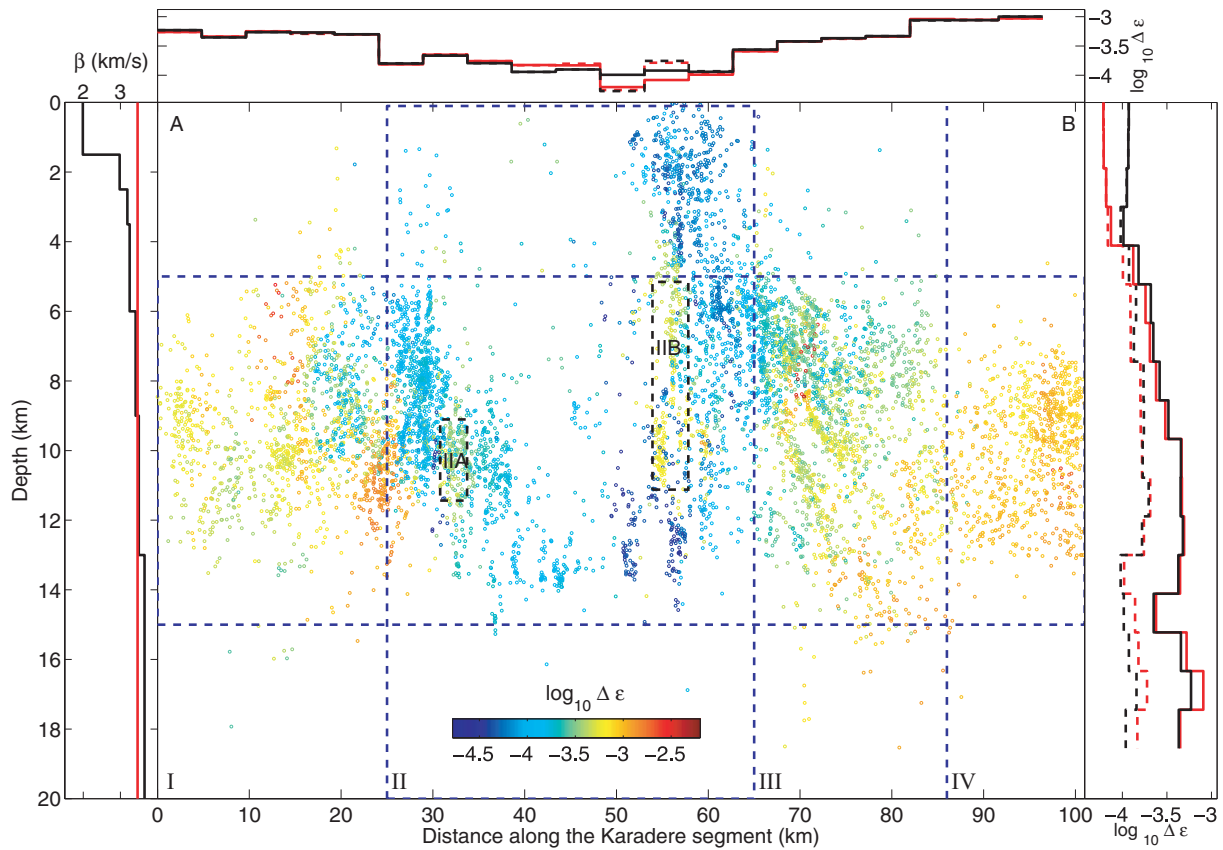
Figure 6. Depth variations of $\log_{10}$ strain-drops along the strike of the seismic lineation in section II (line AB in Fig. 5a). The results are coloured in equal increments of $\log_{10} \Delta\varepsilon$ with colour bar at the bottom. The panel at the left-hand side shows the constant (red line) and 1-D velocity (black line) velocity models. Four different fault sections are separated by vertical dashed lines and the horizontal dashed lines between 5 and 15 km contain the majority of the events. The two off-fault high strain-drop clusters in section II (IIA and IIB) are marked with dashed rectangles. The panel on the top shows the average $\log_{10}$ $\Delta\varepsilon$ versus horizontal coordinate for all events (solid line), as well as for events with depth between 5 and 15 km (dashed lines) for the constant (red) and 1-D (black) velocity models. The right-hand panel shows the average $\log_{10} \Delta\varepsilon$ versus depth in section II (dashed line) and in the whole aftershock zones (solid line) for the constant (red) and 1-D (black) velocity models.

Karadere segment (section II). The distribution of the strain-drops along the vertical plane is shown in Fig. 6. To examine the effects of the assumed constant $\beta = 3.5$ km s^{-1} (red line in the left-hand panel of Fig. 6), we also compute strain-drops with a 1-D velocity model for this region given by black line in the left-hand panel of Fig. 6 (Seeber *et al.* 2000). The average values of the strain-drops versus depth, derived using both velocity models, are plotted in the right-hand panel of Fig. 6. For better spatial resolution, we examine the average depth variation of strain-drops of all events (solid lines) as well as the events occurring only inside section II (dashed lines). The results obtained with the two different velocity models are very similar except for the shallow section. With the 1-D velocity model, the average strain-drops (black lines) in the top 4 km have higher values than those obtained with the constant velocity model (red lines). With the constant velocity model, the average $\log_{10}$ strain-drop of all events increases with depth from −4.2 around 3 km to −3.3 at 10 km depth (corresponding to nominal stress-drops of 1.9 and 15.0 MPa, respectively). The strain-drops inside section II have weak depth dependence with the constant velocity model, and nearly no depth dependence with the 1-D velocity model.

The top panel of Fig. 6 shows variations of the average strain-drops with distance along the line AB of Fig. 5(a), using results obtained with both velocity models. For better spatial resolution,

we present average strain-drops for all events (solid lines) as well as for events in the depth range 5–15 km (dashed lines), where most aftershocks occurred. As mentioned earlier, the strain-drops inside section II are lower compared with those in the other sections. Most of the earthquakes with depth less than 5 km occurred in the top-right-hand portion of section II (NE of station GE in Fig. 1), and most of them have relatively small strain-drop values. The differences somewhat decrease for results based on the 1-D velocity model (black lines), but the overall pattern remains the same.

4.2 Temporal variations of strain-drops

The availability in our data set of both foreshocks and aftershocks of the 1999 Düzce main shock, including many events near the hypocentre of the Düzce main shock, motivates us to search for possible informative temporal evolution of the derived strain-drops. Fig. 7 shows the obtained strain-drop distributions of earthquakes occurring before and after the Düzce main shock. Although the locations and rates of subsets of the seismicity change dramatically (e.g. Peng & Ben-Zion 2005), the overall patterns of strain-drops appear to be relatively stable before and after the occurrence of the Düzce main shock. To further quantify the temporal changes of strain-drops, we study the evolution of $\log_{10}$ strain-drops versus time inside each section (Fig. 8). The median values of strain-drops
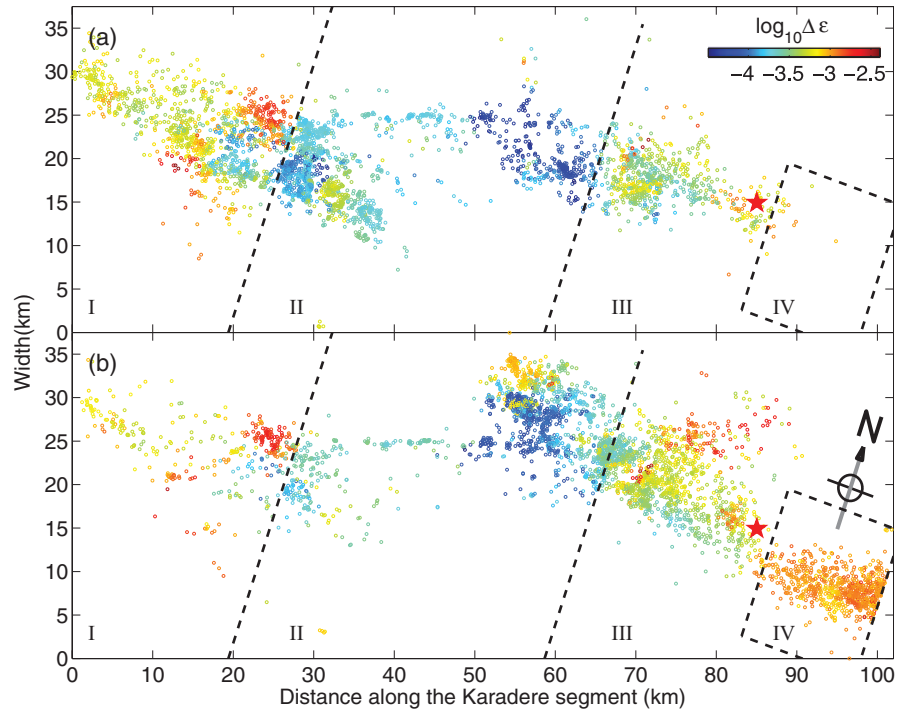
Figure 7. Map views of strain-drops (colour scale) of events before (a) and after (b) the Düzce main shock (red star). The dashed lines separate the sections with labels at the left-hand-bottom corner.

Table 1. Statistical features of the four sub sections.

| Section	I	II	III	IV
Mean $\log_{10} \Delta\varepsilon$	-3.29 ± 0.31	-3.85 ± 0.32	-3.40 ± 0.25	-3.04 ± 0.09
Events Number	1528	3289	1931	750
Mean magnitude	1.73 ± 0.56	1.37 ± 0.63	1.98 ± 0.61	2.29 ± 0.59

(red dashed lines) change after the Düzce main shock in sections I and II, although the differences are within the range of the standard deviation (grey lines) and remain about the same in section III and IV.

One way of delineating the temporal evolution of the shapes of data points associated with groups of events is to plot the 95 per cent bounds of the distributions (e.g. Rolandone *et al.* 2004). However, this method is suited for describing samples that have a large number of events that obey the Gaussian distribution. In our case, the temporal distribution of strain-drops does not satisfy either of these two conditions. Instead, we use the mean of the highest and lowest three strain-drop values in successive time intervals of 8 days (black lines) to delineate the temporal evolution of the strain-drop envelopes. The shapes remain stable when we use mean values based on two and four points instead of three. With this simple method, we observe different temporal characteristics in the strain-drop envelopes at the four different sections. The envelopes for sections I and IV exhibit decays in the range of strain-drops with time from the İzmit and Düzce main shocks. The envelope in section II fluctuates within about constant range, whereas the envelope in section III fluctuates at a constant level before the Düzce main shock and decays thereafter. Since the range of values is expected to increase with increasing number of events (which lead to a more complete sampling of the available distributions), the stability of the strain-drops in section II is somewhat surprising.
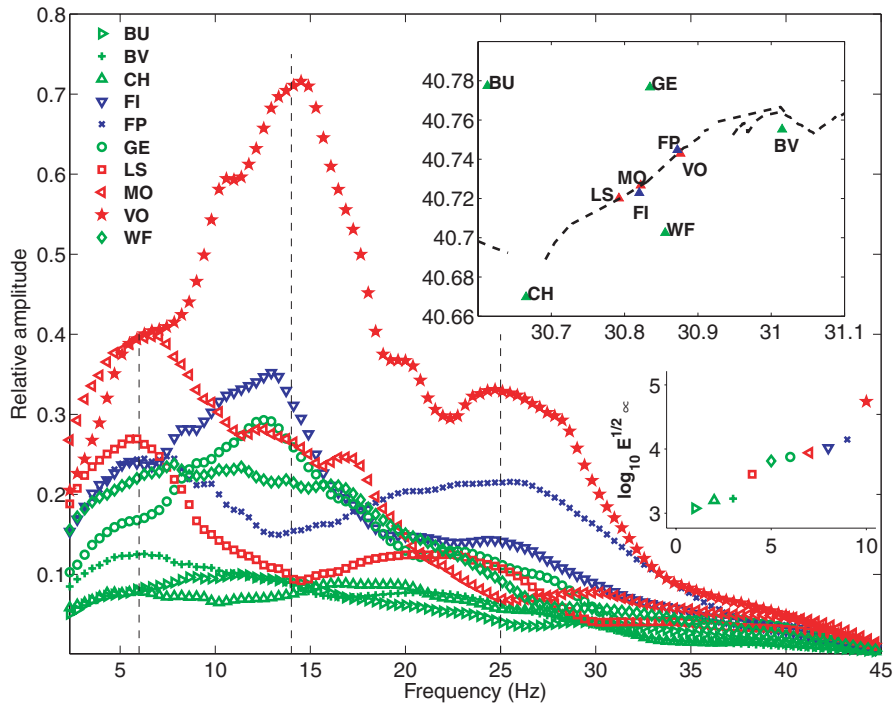
4.3 Station spectral terms

So far we focused on the source spectra and ignored the other terms of eq. (1). Since the seismic network was deployed close to the İzmit rupture zone (Fig. 1), the data provide important opportunity for studying station terms as a function of the distance from the rupture zone. In particular, it is interesting to examine whether the damaged low-velocity fault zone layer that produces seismic trapped waves (Ben-Zion *et al.* 2003) and non-linear wave propagation effects (Karabulut & Bouchon 2007; Wu *et al.* 2009) in the region has a clear signature on the station spectra. Fig. 9 presents a summary of the station spectra obtained by stacking the station terms derived for each event assuming a constant quality factor $Q = 300$. We divide the 10 seismic stations to three general categories based on their distances (top inset of Fig. 9) from the observed rupture traces: within the rupture zones (stations VO, LS and MO; red symbols in Fig. 9), near the rupture zones (stations FI and FP; blue symbols) and away from rupture zone (stations BV, BU, CH, GE and WF; green symbols).

The station spectral shapes are overall relatively smooth, reflecting the fact that each shape is stacked from 7498 separated station terms. We observe three clear peaks in the spectra of various stations around 6, 14 and 25 Hz. The peak frequency around 6 Hz appears most clearly for stations within and near the rupture zones, and it generally decays with distance from the rupture zone. This peak frequency is also observed in the trapped waves study of Ben-Zion
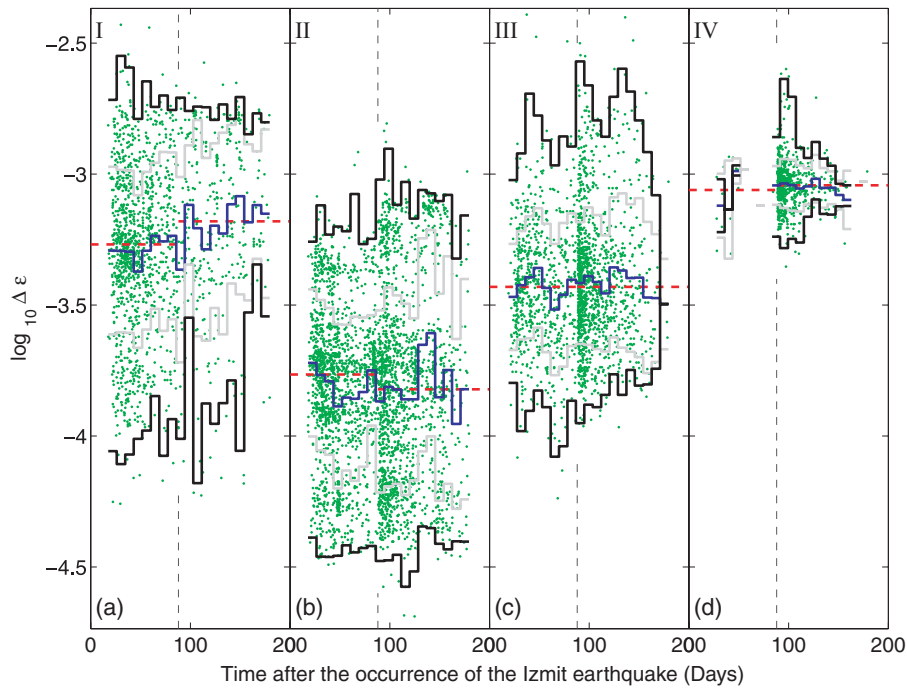
Figure 8. Temporal variations of strain-drops of earthquakes inside section I (a), II (b), III (c) and IV (d). The red dashed lines show the median of $\log_{10}$ strain-drops before and after the occurrence of the Düzce earthquake. The solid blue lines in the middle and the grey lines above and below it are the median value of $\log_{10} \Delta \varepsilon$ and corresponding ranges of standard deviations in 8-day intervals. The solid black lines are used to delineate the temporal variations of the strain-drops in each section. The vertical dashed lines in each subplot mark the time of the Düzce main shock.

Figure 9. Stacked station spectra terms. The vertical dashed lines mark peak frequencies that are shown in various stations. The inset top-right-hand panel shows the distribution of stations (triangles) in relation to observed rupture traces (black dashed line). The lower inset gives the integral of the site spectral energy for each station. The employed colours for stations and spectra (legend at the top-left-hand corner) are based on distances from the rupture traces: red – within the rupture zone; blue – within 500 m from the rupture zone and green – more than 1.0 km from the rupture zone.

et al. (2003) using shear waveforms in the same region, as well as the trapped *S* waves studies near the rupture zone of the 1992 Landers earthquake (Peng *et al.* 2003) and the San Jacinto fault in California (Lewis *et al.* 2005). These studies also show that the spectral amplitude around this peak is inversely correlated with the distance from the rupture trace. The other two peaks around 14 and 25 Hz are seen clearly at a mixture of stations. Stations VO and FI, which are within or near the fault zone and off-fault station GE

have a clear peak frequency near 14 Hz, and their highest spectral amplitudes are associated with that peak. The 25 Hz peak frequency is present at stations VO, FI, FP and LS, which are within or near the rupture zone. The large spectral peak at 14 Hz in the records of stations VO and FI may reflect a damaged fault zone layer that is observed in the *P* wave analysis of this work and is probably narrower than the trapping structure of the shear waves. The origin of the 14 Hz spectral peak at station GE and the fact that fault zone station MO does not have spectral peaks at 14 and 25 Hz remain, at present, unclear. Further observations and analyses are needed to better explain these results.

The 'site energy' contained in the different station spectral terms can be estimated by $\int [2\pi f u(f)]^2 \mathrm{d}f$, giving the integrated square of the station displacement spectra over the examined frequency range. The inset in the low-right-hand portion of Fig. 9 gives the obtained $\log_{10}$ squared root values of the station spectral terms integrated over the frequency range 2.35–30 Hz. The data of station VO that is within the highly damaged rupture zone have the largest site energy, whereas the seismic records at the off-fault stations BU, CH and BV have the smallest site energies. The order of the site energies of the other stations does not show a clear relation to the distance from the fault and is probably associated with various local site effects.

5 DISCUSSION

A major general goal of earthquake seismology is to establish connections between properties of fault zone structures, properties of earthquake sources on the faults and generated seismic radiation at various stations. In this work, we derived source, traveltime and station spectra for groups of earthquakes from observed *P* waves of 7498 events in the aftershock zones of the 1999 İzmit and Düzce earthquakes along the Karadere-Düzce branch of the NAF. The analysis is based on the procedure of Shearer *et al.* (2006) with small modifications, and employs data-stacking multiple times. At the iterative separation of the source, station and traveltime terms (Section 3.1), the observed source spectra of 201 nearest neighbouring events, recorded by various stations and shared within given epicentral distance intervals, are stacked. In Section 3.2, the separated source terms are stacked within given amplitude bins. At the strain-drop fitting stage (Section 3.3), the differences between binned separated source spectra and theoretical source spectra are stacked to form a common EGF. Through stacking, random noise in each individual spectrum is largely suppressed and the common features of the source, traveltime and station spectra are highlighted. However, the stacking may also suppress genuine internal variations of properties, and it limits the resolution of the results to common properties of the used groups of events.

We fit earthquake strain-drops from the separated source spectra with the ω^{-2} source model. The mean of the $\log_{10}$ of strain-drop for the data is –3.5 (corresponding to a mean stress drop value of 9.5 MPa). The spatial distributions of seismicity and derived strain-drops can be used, along with the overall geometrical properties of the faults, to divide the study area into four sections (Figs 5–7). The distributions of strain-drops show temporal evolutions that probably reflect primarily the temporal changes in the numbers of events (Fig. 8). The ranges of the derived values are larger in the early time of the aftershock sequences and decay gradually with time. In some sections, there are small step-like changes in the average strain-drop values across the time of the Düzce main shock, but the results are within the standard deviations and may not be statistically significant.

Using a constant velocity model, Shearer *et al.* (2006) found that the median stress-drops of earthquakes in southern California increases with depth from 0.6 MPa near the surface to 2.2 MPa at 8 km. Our results from the İzmit-Düzce aftershock zones with a constant velocity model show a similar pattern, with larger changes of values, in which the mean $\log_{10}$ strain-drops of all events increases from −4.2 (1.9 MPa) at 0–4 km depth to −3.3 (15.0 MPa) at 10 km depth. We note that the strain-drops over the depth range 0–4 km are associated primarily with events in region IIB (NW of station GE), but the overall tendency of strain-drops to increase with depth between 4 and 10 km is a general characteristic of the different regions. Fletcher & McGarr (2006) inferred from analysis of slip models that stress drops increase from 10 MPa at 6 km to 43 MPa at 16.5 km for the Northridge earthquake, and from 7 MPa at 1.5 km to 20 MPa at 6.2 km for the Landers earthquake. Allmann & Shearer (2007) showed that the depth dependence of stress drops in the Parkfield section of the San Andres Fault disappears when a more accurate depth-dependent velocity model replaces the constant velocity model.

To test if the depth variations of our derived strain-drops are controlled by the velocity model, we recomputed the strain-drops with a 1-D velocity model for the study area (black line in left-hand panel of Fig. 8). Although the derived $\log_{10}$ strain-drop values change somewhat, the overall pattern of increasing strain-drops with depth remains. The derived values of strain-drops are likely to change further if we use a 3-D velocity model. In particular, additional reductions of the shallow *S*-wave velocities would increase the derived shallow strain-drops and reduce the overall change of strain-drops with depth. However, the employed 1-D velocity model probably captures the overall depth variations of velocities, and the obtained increasing strain-drops with depth likely reflect, at least partially, the increasing confining pressure with depth and the reduction of the stored elastic strain toward the surface and the brittle–ductile transition.

The properties of earthquakes along the relatively straight Karadere segment in section II are different in many aspects from those of earthquakes in the other sections (Figs 5–8). Seismotectonically, sections I and III are inside the extensional Akyazi and Düzce basin, respectively. Both basins belong to a series of active pull-apart structures from Düzce to the Sea of Marmara (e.g. Sengor *et al.* 2005). The dominant focal mechanisms in sections I and III are normal, and the dominant focal mechanisms along the Karadere segment in section II are strike-slip (Bohnhoff *et al.* 2006). The rupture zone of the İzmit earthquake changes its strike from nearly EW in the Akyazi basin to N71°E along the Karadere segment. The rupture zone of the Düzce earthquake changes back to nearly EW direction in the Düzce basin. We note that abundant aftershocks tend to concentrate near stations CH and BV where the fault rupture changes its strike, probably due to reactivations of secondary normal faults by stress concentrations near abrupt changes in the geometry of the main shock ruptures. The low strain-drops inside section II probably reflect the geometrical simplicity (and hence reduced stress concentrations) along that section. Compared with the clear lineation of microseismicity inside section II, the earthquake distributions in sections I, III and IV are considerably more distributed, implying strong geometrical heterogeneities. Additional evidence of fault heterogeneity could be derived from the range of event sizes, which should become broader as the fault structures become more heterogeneous (Ben-Zion 1996; Zöller *et al.* 2005). This is consistent with the fact that the maximum magnitude is the smallest in section II among all sections.

The analysis of the stacked station spectra indicates strong variations of site effects and three frequencies with clear peak amplitudes that are observed at various stations (Fig. 9). The amplitude of the station spectra are generally inversely correlated with the distance to the rupture traces up to a frequency of about 6 Hz, where all station spectra have either a peak or an inflexion point. Some of the stations have peak spectral amplitudes around 14 and 25 Hz. The peaks at 6 and 14 Hz may be related to fault zone trapped waves in the *S* and *P* portions of the seismograms, respectively. The integral of the station spectra over the frequency range 2.35–30 Hz is largest for the fault zone station VO, which records clear trapped waves and temporal changes of properties (Ben-Zion *et al.* 2003; Peng & Ben-Zion 2006; Wu *et al.* 2009), and smallest for the off-fault stations BU, CH and BV. The derived patterns of source and site terms should be substantiated by additional results based on *S* waveforms and other types of analysis. This will be done in future work.

REFERENCES

Abercrombie, R., 1995. Earthquake source scaling relationships from −1 to 5 M_L using seismograms recorded at 2.5 km depth, *J. geophys. Res.,* **100,** 24 015–24 036.

Allmann, B.P. & Shearer, P.M., 2007. Spatial and temporal stress drop variations in small earthquakes near Parkfield, California, *J. geophys. Res.,* **112,** B04305, doi:10.1029/2006JB004395.

Aki, K. & Richards, P.G., 2002. *Quantitative Seismology,* University Science Books, Sausalito, CA.

Andrews, D.J., 1986. Objective determination of source parameters and similarity of earthquakes of different size, in *Earthquake Source Mechanics,* Vol. 37, pp. 259–267, eds Das, S., Boatwright, J. & Scholz, C.H., *American Geophysical Union Monograph.*

Ben-Zion, Y., 1996. Stress, slip, and earthquakes in models of complex single-fault systems incorporating brittle and creep deformations, *J. geophys. Res.*, **101,** 5677–5706.

Ben-Zion, Y., 2003. Appendix 2: key formulas in earthquake seismology, in *International Handbook of Earthquake and Engineering Seismology,* Part B, pp. 1857–1875, eds HK Lee, W., Kanamori, H., Jennings, P.C. & Kisslinger, C., Academic Press, Boston, MA.

Ben-Zion, Y., 2008. Collective behavior of earthquakes and faults: continuum-discrete transitions, evolutionary changes and corresponding dynamic regimes, *Rev. Geophys.,* **46,** RG4006, doi:10.1029/ 2008RG000260.

Ben-Zion, Y. & Zhu, L., 2002. Potency-magnitude Scaling Relations for Southern California Earthquakes with $1.0 < M_L < 7.0$, *Geophys. J. Int.,* **148,** F1–F5.

Ben-Zion, Y. *et al.*, 2003. A shallow fault-zone structure illuminated by trapped waves in the Karadere-Düzce branch of the North Anatolian Fault, western Turkey, *Geophys. J. Int.,* **152,** 699–717.

Berckhemer, H., 1962. Die Ausdehnung der Bruchfläche im Erdbebenherd und ihr Einfluss auf das seismische Wellenspektrum, *Gerlands Beitr. Geophys.*, **71,** 5–26.

Boatwright, J., Fletcher, J.B. & Fumal, T.E., 1991. A general inversion scheme for source, site, and propagation characteristics using multiply recorded sets of moderate-sized earthquakes, *Bull. seism. Soc. Am.,* **81,** 1754–1782.

Bohnhoff, M., Grosser, H. & Dresen, G., 2006. Strain partitioning and stress rotation at the North Anatolian Fault after the 1999 İzmit $M_W = 7.4$ earthquake, *Geophys. J. Int.,* **166,** 373–385.

Brune, J.N., 1970. Tectonic stress and the spectra of seismic shear waves from earthquakes, *J. geophys. Res.,* **75,** 4997–5009.

Creager, K.C., 1997, Coral, *Seism. Res. Lett.,* **68,** 269–271.

Fletcher, J.B. & McGarr, A., 2006. Distribution of stress drop, stiffness, and fracture energy over earthquake rupture zones, *J. geophys. Res.,* **111,** B03312, doi:10.1029/2004JB003396.

Hough, S.E., 1997. Empirical Green's function analysis: taking the next step, *J. geophys. Res.,* **102,** 5369–5384.

Ide, S. & Beroza, G.C., 2001. Does apparent stress vary with earthquake size?, *Geophys. Res. Lett.*, **28**(17), 3349–3352.

Karabulut, H. & Bouchon, M., 2007. Spatial variability and non-linearity of strong ground motion near a fault, *Geophys. J. Int.,* **170,** doi:10.1111/j.1365-246X.2007.03406.x

Lewis, M.A., Peng, Z., Ben-Zion, Y. & Vernon, F.L., 2005. Shallow seismic trapping structure in the San Jacinto fault zone near Anza, California, *Geophys. J. Int.,* **162,** 867–881, doi:10.1111/j.1365-246X.2005.02684.x.

Park, J., Lindberg, C.R. & Vernon, F.L., 1987. Multitaper spectral analysis of high frequency seismograms, *J. geophys. Res.,* **92,** 12 675–12 648.

Prieto, G., Shearer, P.M., Vernon, F.L. & Kilb, D., 2004. Earthquake source scaling and self–similarity estimation from stacking P and S spectra, *J. geophys. Res.,* **109,** B08310, doi:10.1029/2004JB003084.

Peng, Z. & Ben-Zion, Y., 2004. Systematic analysis of crustal anisotropy along the Karadere-Düzce branch of the north Anatolian fault, *Geophys. J. Int.,* **159,** 253–274.

Peng, Z. & Ben-Zion, Y., 2005. Spatio-temporal variations of crustal anisotropy from similar events in aftershocks of the 1999 *M*7.4 İzmit and *M*7.1 Düzce, Turkey, earthquake sequences, *Geophys. J. Int.,* **160,** 1027–1043.

Peng, Z. & Ben-Zion, Y., 2006. Temporal changes of shallow seismic velocity around the Karadere-Düzce branch of the north Anatolian fault and strong ground motion, *Pure appl. Geophys.,* **163,** 567–600.

Peng, Z., Ben-Zion, Y., Michael, A.J. & Zhu, L., 2003. Quantitative analysis of seismic trapped waves in the rupture zone of the 1992 Landers, California earthquake: Evidence for a shallow trapping structure, *Geophys. J. Int.,* **155,** 1021–1041.

Madariaga, R., 1976. Dynamics of an expanding circular fault, *Bull. seism. Soc. Am.,* **66,** 639–666.

Mueller, C.S., 1985. Source pulse enhancement by deconvolution of an empirical Green's function, *Geophys. Res. Lett.,* **12,** 33–36.

Rolandone, F., Bürgmann, R. & Nadeau, R.M., 2004. The evolution of the seismic-aseismic transition during the earthquake cycle: constraints from the time-dependent depth distribution of aftershocks, *Geophys. Res. Lett.,* **31,** L23610, doi:10.1029/2004GL021379.

Seeber, L. *et al.*, 2000. The 1999 earthquake sequence along the North Antolian Transform at the juncture between the two main ruptures, in *The 1999 İzmit and Düzce Earthquakes: Preliminary Results,* Special Volume, eds Barka, A., Kozaci, O., Akyuz, S. & Altunel, S., ITU, Istanbul.

Sengor, A.M.C. *et al.*, 2005. The North Anatolian Fault: a new look, *Ann. Rev. Earth planet. Sci.,* **33,** 37–112, doi:10.1146/annurev.earth.32.101802.120415.

Shearer, P., Prieto, G. & Hauksson, E., 2006. Comprehensive analysis of earthquake source spectra in southern California, *J. geophys. Res.*, **111,** B06303, doi:10.1029/2005JB003979.

Thomson, D.J., 1982. Spectrum estimation and harmonic analysis, *Proc. IEEE.*, **70,** 1055–1096.

Warren, L.M. & Shearer, P.M., 2002. Mapping lateral variations in upper mantle attenuation structure by stacking P and PP spectra, *J. geophys. Res.,* **107**(B12), 2342, doi:10.1029/2001JB001195.

Wu, C., Peng, Z. & Ben-Zion, Y., 2009. Non-linearity and temporal changes of fault zone site response associated with strong ground motion, *Geophys. J. Int.*, **176,** 265–278, doi:10.1111/j.1365-246X.2008.04005.x.

Zöller, G., Holschneider, M. & Ben-Zion, Y., 2005. The role of heterogeneities as a tuning parameter of earthquake dynamics, *Pure appl. Geophys.,* **162,** 1027–1049.